

High-Reversibility Sulfur Anode for Advanced Aqueous Battery

Qianru Chen, Junnan Hao, Shaojian Zhang, Zhihao Tian, Kenneth Davey, and Shi-Zhang Qiao*

Despite being extensively explored as cathodes in batteries, sulfur (S) can function as a low-potential anode by changing charge carriers in electrolytes. Here, a highly reversible S anode that fully converts from S_8^0 to S^{2-} in static aqueous $S-I_2$ batteries by using Na^+ as the charge carrier is reported. This S anode exhibits a low potential of -0.5 V (vs standard hydrogen electrode) and a near-to-theoretical capacity of 1404 mA h g^{-1} . Importantly, it shows significant advantages over the widely used Zn anode in aqueous media by obviating dendrite formation and H_2 evolution. To suppress “shuttle effects” faced by both S and I_2 electrodes, a scalable sulfonated polysulfone (SPSF) membrane is proposed, which is superior to commercial Nafion in cost (US\$1.82 m^{-2} vs \$3500 m^{-2}) and environmental benignity. Because of its ultra-high selectivity in blocking polysulfides/iodides, the battery with SPSF displays excellent cycling stability. Even under 100% depth of discharge, the battery demonstrates high capacity retention of 87.6% over 500 cycles, outperforming Zn- I_2 batteries with 3.1% capacity under the same conditions. These findings broaden anode options beyond metals for high-energy, low-cost, and fast-chargeable batteries.

1. Introduction

Sulfur (S) cathodes are considered competitive because of their inherently high capacity of 1675 mA h g^{-1} , natural abundance (ranked 16th in Earth crust), and low cost of 52 A h $\$^{-1}$.^[1] However, the use of organic electrolytes in S-based batteries can result in practical difficulty because of flammability, high cost, and poor ionic conductivity.^[2] To obviate these, aqueous systems have been developed by coupling S electrodes with water-compatible metal anodes. For example, S electrode has been used as cathode in Zn metal batteries and the discharge product of S, S^{2-} ions, coordinates with Zn^{2+} to form solid-state ZnS. The cathode conversion mechanism therefore is $S(s) \leftrightarrow ZnS(s)$ reaction with a redox potential of 0.22 V (vs standard hydrogen electrode (SHE)).^[3] This battery, however, exhibits significant polarization of 1.0 V

and an unacceptably low discharge plateau of ≈ 0.3 to 0.4 V even at a low rate of 0.1 A g^{-1} . This is attributed to sluggish reaction kinetics and poor electronic conductivity of S_8^0 (5×10^{-28} S m^{-1}) and ZnS (10^{-9} S m^{-1}).^[3a] Similarly, Fe-S, Cu-S, and Pb-S batteries have also been reported.^[4] However, the discharge plateaus are within 0.1 to 0.3 V because of the narrow potential gap between the S/M_xS conversion ($M = Fe, Cu, Pb; x = 1$ or 2) and the counter M/M^{2+} or M^{2+}/MO_2 reaction, significantly decreasing energy density of S-based batteries.

$Li^+/Na^+/K^+$ charge carriers in aqueous electrolytes can benefit the redox kinetics of S electrode because of liquid-liquid reactions of short-chain polysulfide conversions ($M_2S_4 \leftrightarrow M_2S_3 \leftrightarrow M_2S_2 \leftrightarrow M_2S$, $M = Li, Na, K$) that enable rapid electron transfer.^[5] With a redox potential of -0.5 V (vs SHE), the S electrode exhibits practical potential as an anode in

aqueous media. Compared to the widely reported Zn anode, the S electrode exhibits significant advantages including, 1) the capacity of S is more than double that for Zn of 820 mA h g^{-1} and 2) it costs only $\$0.106$ kg^{-1} , which is $1/37$ th the cost of Zn at $\$3.95$ kg^{-1} . Furthermore, the Zn anode is prone to dendritic growth and the hydrogen evolution reaction (HER), a side reaction in aqueous solutions. These factors pose a significant risk to battery stability and safety.^[6] Zn metal also acts as both current collector and active material, making it practically difficult to operate under high utilization.^[7] The Zn electrode reportedly operates at $<1\%$ depth of discharge (DoD), which represents the fraction of the electrode capacity that has been used. This low Zn utilization substantially diminishes battery energy density and provides limited potential for practical application.^[8] In contrast, the S anode obviates dendrites and HER and can realize 100% utilization (Figure 1a). The S electrode therefore appears to be a highly desirable alternative to the Zn electrode, offering high capacity, high utilization, and low cost in aqueous media.

However, the S/M_2S ($M = Li, Na, K$) reaction in aqueous media is practically challenging because of the “shuttle effects” of soluble polysulfide intermediates that result in decreased Coulombic efficiency (CE) and shortened cycle life.^[9] Reported strategies of porous carbon encapsulation and conductive polymer coating^[10] can only enable S electrode to achieve a low cycling capacity of <200 mA h g^{-1} , significantly lower than its theoretical value. This is possibly because the small size of soluble short-chain polysulfides makes it difficult for them to be confined within a carbon

Q. Chen, J. Hao, S. Zhang, Z. Tian, K. Davey, S.-Z. Qiao
School of Chemical Engineering
The University of Adelaide
Adelaide, SA 5005, Australia
E-mail: s.qiao@adelaide.edu.au

The ORCID identification number(s) for the author(s) of this article can be found under <https://doi.org/10.1002/adma.202309038>

© 2023 The Authors. Advanced Materials published by Wiley-VCH GmbH. This is an open access article under the terms of the Creative Commons Attribution License, which permits use, distribution and reproduction in any medium, provided the original work is properly cited.

DOI: 10.1002/adma.202309038

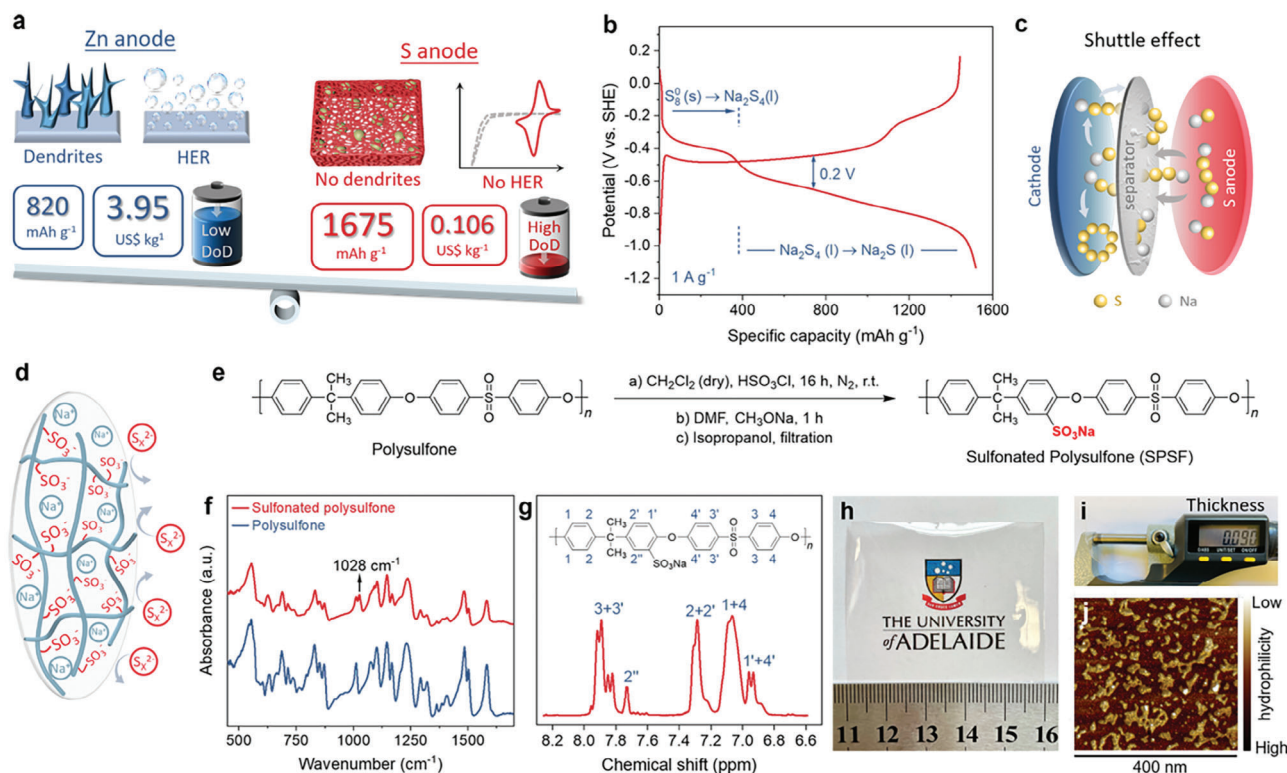


Figure 1. Electrochemistry and practical challenge of sulfur (S) anode, and membrane synthesis and characterization. a) Comparison of Zn anode and S anode. b) Charge-discharge curves of S electrode at 1 A g⁻¹. c) Shuttle effects of polysulfides in S anode-based aqueous battery. d) Schematic for cation exchange membrane structures. e) Synthetic route for SPSF. f) FTIR spectra for polysulfone before and after sulfonation. g) ¹H NMR spectrum for SPSF. h) Digital image of SPSF membrane with a size of 5.0 × 5.0 cm. i) Thickness of SPSF membrane determined by electronic spiral micrometer (unit = mm). j) AFM phase image of SPSF membrane following soaking in deionized water.

or polymer matrix. A potential solution is to regulate the electrolyte to prevent dissolution of polysulfides and impede shuttling, as is reported with “water-in-bisalt” gel electrolytes, which are highly concentrated semi-solid electrolytes.^[11] However, the super-concentrated fluoride salts significantly boost the cost for practical applications. Moreover, the quasi-solid electrolyte reduces the ionic conductivity, resulting in a low battery rate of 1 C. Alternatively, cation exchange membranes, known for their selective cation permeability, can be used to block polysulfides, as evidenced by commercial Nafion membranes.^[9,12] However, the use of Nafion is impractical for grid-level energy storage due to its high cost of >\$3500 m⁻² and the associated environmental risk posed by its by-products, perfluoroalkyl and polyfluoroalkyl substances, known as “permanent chemicals” that can contaminate drinking water to threaten human health.^[13] Hence, there is a need for a practical, low-cost, and environmentally benign approach to suppress shuttle effects of S anode.

Here, we report a highly reversible S anode for static aqueous S-I₂ battery by designing a low-cost and high-safety cation exchange membrane of sulfonated polysulfone (SPSF). In contrast to commercial Nafion, this SPSF membrane is, 1) made from a nonfluorinated hydrocarbon polymer, polysulfone, which is environmentally benign and significantly more cost-effective, costing only 0.052% of Nafion and, importantly, 2) its high cation selectivity outperforms Nafion, allowing the S-I₂ battery to exhibit a near-to-theoretical capacity of 1404 mA h g⁻¹, together

with a high CE of 95.2%. At a record-breaking rate of 8 C (13.4 A g⁻¹), the battery maintains a high capacity of 744 mA h g⁻¹ and exhibits significant cycling stability with 99.95% capacity retention per cycle. Importantly, when operating under harsh conditions of semi- to full utilization of S (50% to 100% DoD), the battery retains 98.1% to 87.6% capacity over 500 cycles, in contrast to Zn-I₂ battery with 28.9% to 3.1% capacity retention. Moreover, the energy density of the S-I₂ battery at 100% DoD is 168.8 W h kg⁻¹, a value significantly greater than reported for aqueous Li/Na/K/Ca/Mg/Zn-based batteries. Findings can be used to practically develop advanced aqueous batteries with high-capacity S anode.

2. Results and Discussion

To confirm practicality of S/M₂S (M = Li, Na, K) electrochemistry in aqueous media, Na⁺ was selected as charge carrier to generate representative charge-discharge curves for S electrode (Figure 1b). S electrochemistry exhibits high reversibility with a narrow charge-discharge gap of only 0.2 V at 1 A g⁻¹, significantly less than the polarization of 1.5 V in Zn-S battery performed at the same rate (Figure S1, Supporting Information), evidencing better reaction kinetics. The reaction potential is -0.5 V versus SHE, confirming its potential to act as an anode in aqueous media. The curve exhibits two platforms, representing transformation from, 1) S₈⁰ (s) to Na₂S₄ (l) and 2) Na₂S₄ (l) to Na₂S

(l), respectively.^[1a,5b] The short-chain polysulfides (Na_2S_x , $1 \leq x \leq 4$) are highly soluble in aqueous solutions ($>2.3 \text{ M}$) and readily migrate toward the cathode, a phenomenon known as “shuttle effects” that lead to capacity loss and CE reduction (Figure 1c).^[14] Utilizing merely solid–solid conversion ($\text{S}_8^0 \leftrightarrow \text{Na}_2\text{S}_5$) can circumvent this issue; however, it comes at the cost of a notable reduction in capacity to 335 mA h g^{-1} . Furthermore, the rapid kinetics associated with liquid–liquid conversion remain untapped. Therefore, in order to fully unlock the potential of sulfur, it is imperative to address the shuttle effects and realize the complete conversion from S_8^0 to Na_2S .

To inhibit the shuttling of polysulfides, a cation exchange membrane was synthesized via attaching negatively charged sulfonate groups to an insoluble polymer backbone (Figure 1d). Polysulfone was selected as the polymer framework due to its ease of processing, cost-effectiveness ($\$17.8 \text{ kg}^{-1}$, equivalent to $\$1.82 \text{ m}^{-2}$ of membrane), and more importantly, its well-established resistance to alkaline conditions.^[15] The introduction of sulfonation groups into polysulfone involved three steps: 1) sulfonation by chlorosulfuric acid, 2) neutralization with sodium methoxide in dimethylformamide, and 3) precipitation with aid of isopropanol (Figure 1e, see Supporting Information for details). The resulting SPSF powders were dissolved in dimethylformamide to generate the membrane solution. The mixture was poured onto a glass dish for solvent evaporation. A self-standing membrane was obtained and peeled off the glass. The sulfonation of polysulfone was confirmed via Fourier transform infrared spectrum (FTIR, Figure 1f), which exhibits a new peak at 1028 cm^{-1} , corresponding to symmetric $\text{O}=\text{S}=\text{O}$ stretching of $-\text{SO}_3\text{Na}$.^[16] This sulfonation structure was further evidenced via ^1H NMR in which proton resonance at $\approx 7.73 \text{ ppm}$ is assigned to the proton adjacent to the sulfonation group (Figure 1g).^[17] Digital images show the membrane is transparent with a thickness of $90 \mu\text{m}$ (Figure 1h,i). Importantly, a large-size membrane with $28.5 \text{ cm} \times 13.5 \text{ cm}$ was also prepared (Figure S2, Supporting Information), confirming mass producibility even in laboratory settings. To establish mechanical strength, a stress–strain test was carried out (Figure S3, Supporting Information), showing that the membrane has robust mechanical property with a high tensile strength of 12.5 MPa . The internal microstructures, especially the ion channels, were established via atomic force microscopy (AFM). It is widely reported that the ion channels in membrane are formed via aggregation of hydrophilic sulfonic groups which are responsible for its ionic conductivity.^[18] In Figure 1j, the bright-color regions are assigned to hydrophobic fields involving the polymer framework, while the dark are hydrophilic domains made from clusters of sulfonic groups.^[18,19] The phase separation is apparent with the dark channels well-connected, allowing for smooth ion conduction.

To assemble a full battery, iodine (I_2) was used as the cathode because of its affordability, high capacity (211 mA h g^{-1}), fast kinetics, and natural abundance ($50\text{--}60 \text{ mg L}^{-1}$ in oceans).^[20] Similar to the S electrode, the I_2 electrode suffers from shuttle effects of soluble intermediates (I_3^-), which can further examine the anion-blocking performance of the SPSF membrane. The S-I_2 redox pair has been proposed for flow batteries. However, only partial S conversion from S^{2-} to S_2^{2-} or S_2^{2-} to S_4^{2-} was reported, and DoD was mostly $<50\%$ (Table S1, Supporting Information).^[14b,21] In our static S-I_2 battery, the conversion

from S to S^{2-} is fully used and DoD is boosted to 100%. In addition, compared with flow batteries that require tanks, pumps, sensors, and flow management, the static cell configuration is significantly simpler and more facile. The coupling of earth-abundant S and I_2 , together with cost-saving SPSF membrane, has apparent practical potential for grid-level energy storage (Figure 2a).

To confirm the practicality of using S and I_2 in a static battery, a three-electrode cell was used to conduct cyclic voltammetry. Findings evidence that both S anode and I_2 cathode exhibit highly reversible redox behavior with narrow peak-to-peak separations, underscoring fast kinetics (Figure 2b). The oxidation peak for S appears at -0.45 V , and reduction peak for I_2 is located at 0.47 V , providing a theoretical working voltage of 0.92 V . To ensure effectiveness of the SPSF membrane in the battery, the sulfonation degree must be optimized. A high sulfonation degree can increase cation flux and thereby decrease membrane resistance and battery polarization. However, an excessive sulfonation degree can cause swelling of ion channels, resulting in the leakage of anions, reduced ion selectivity, and decreased battery efficiency.^[22] To establish the optimal sulfonation degree, selected levels of sulfonation ranging from 13% to 78%, were tested using the laboratory-made battery (Figures S4–S6, Supporting Information). Findings confirm that increasing degree of sulfonation reduces polarization from 1.41 to 0.14 V . However, it also results in a decrease in CE from 100% to 58.6%. A sulfonation degree of 55% is selected for subsequent battery tests because it provides a moderate polarization of 0.31 V and a high initial CE of 96.5% at 2 C (Figure S7, Supporting Information).

Battery performance with the optimized SPSF membrane was compared to those with commercial Nafion 117 (N117) and conventional glass fiber (GF). The SPSF-based battery exhibits a high discharge capacity of 1404 mA h g^{-1} with an initial CE of 95.2% and a low polarization of 0.18 V at 0.5 C (Figure 2c). The discharging voltage of 0.91 V is close to the theoretical value. In contrast, the battery with N117 exhibits a reversible capacity of only 724 mA h g^{-1} with an initial CE of 52.6% under the same conditions. The GF-based battery shows a low discharge capacity of 127 mA h g^{-1} with a significantly low CE of 16.4%, evidencing poor performance in blocking shuttle effects of both polysulfides and polyiodides. The SPSF-based battery exhibits a capacity of 1400 mA h g^{-1} at 1 C (Figure 2d). At increased current rates, the capacity decreases to 1211.9, 1115.5, 973.8, and $856.2 \text{ mA h g}^{-1}$ at, respectively, 2 C , 3 C , 4 C , and 5 C . When the rate returns to 1 C , the capacity increases to $1206.2 \text{ mA h g}^{-1}$. In comparison, the capacity of the N117-based battery is $1120.4 \text{ mA h g}^{-1}$ at 1 C in the first cycle, and it decreases to $699.3 \text{ mA h g}^{-1}$ after ten cycles. As the rate gradually increases, the capacity decreases to, respectively, 627.6, 527.8, 471.3, and $430.4 \text{ mA h g}^{-1}$ at 2 C , 3 C , 4 C , and 5 C , a value approximately a half that for the SPSF battery. The battery recovers to $524.4 \text{ mA h g}^{-1}$ capacity after returning to 1 C rate. The GF-based battery only realizes $169.1 \text{ mA h g}^{-1}$ at 1 C and rapidly decreases to 43.2 mA h g^{-1} within ten cycles. It is concluded that SPSF exhibits superior performance in confining polysulfide and polyiodide ions compared with N117 and GF separators. Representative charge–discharge curves for the three batteries under selected rates are shown in Figure 2e and Figures S8 and S9 in the Supporting Information. Figure 2e evidences that the SPSF-based battery has a working voltage of

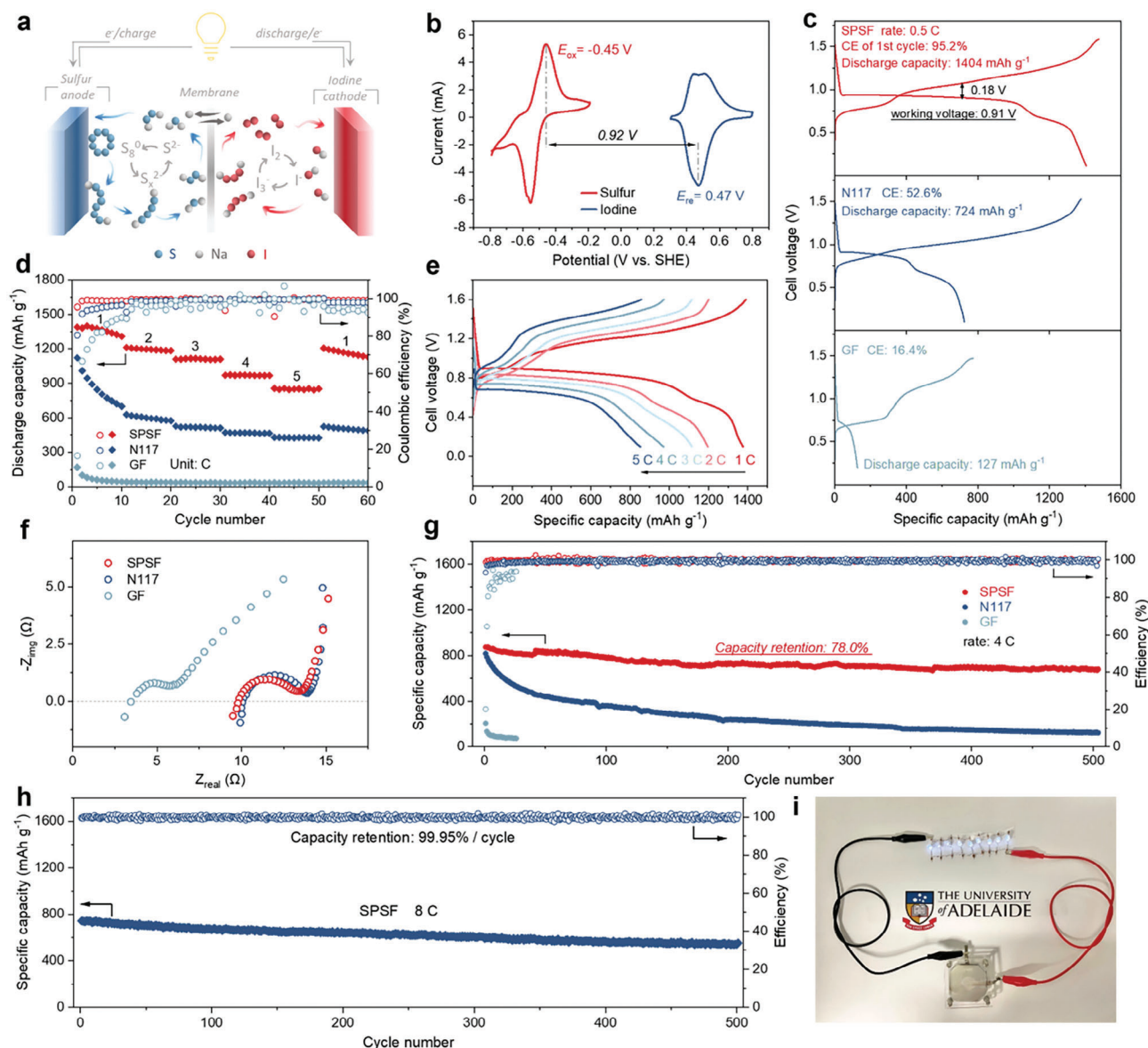


Figure 2. Performance of S-I₂ full cell. a) Schematic showing function of SPSF membrane in S-I₂ battery. b) Cyclic voltammetry of S and I₂ electrodes in a three-electrode system under 1 mV s⁻¹. c) Charge-discharge profiles and d) rate performance of S-I₂ batteries with different membranes. e) Representative charge-discharge curves of the battery with SPSF at selected rates. f) EIS spectra of batteries with different membranes at frequency ranging from 1 Hz to 1 MHz (effective membrane area = 0.38 cm²). Cycling performance of g) the S-I₂ batteries with membranes at 4 C and h) SPSF-based battery at higher rate of 8 C. i) Digital image of S-I₂ battery stack with three single cells in series that powered nine light emitting diodes (LEDs, 2.0 V).

0.83 V at 1 C and remains at 0.63 V at 5 C, confirming fast kinetics.

Selectivity of the membrane for cations improves battery efficiency, but it also leads to an increase in ohmic resistance due to restriction of anion conduction. To measure the ohmic resistance of different batteries, electrochemical impedance spectroscopy (EIS) was carried out to give Nyquist plots (Figure 2f). Based on horizontal intercepts, the GF-based battery has the lowest ohmic resistance at 3.4 Ω, while the SPSF and N117-based batteries have significantly greater resistance at, respectively, 9.8 and 10.1 Ω. The SPSF-based battery has a lower ohmic impedance

than the N117-based battery, evidencing a higher conductivity of the SPSF membrane, as proved in Figure S10 in the Supporting Information. Given that the SPSF-based battery exhibits a higher efficiency, it is apparent that the SPSF membrane has an overall better balance between ion selectivity and permeability.

To evaluate cycling stability of different batteries, galvanostatic charge-discharge tests were conducted at 4 C for 500 cycles (Figure 2g). The 1) N117-based battery exhibits a significant capacity fading within the first 50 cycles and then decreases gradually to 14.8% capacity, 2) GF-based battery exhibits poorer performance with an initial capacity of 206.8 mA h g⁻¹ that

decreases to 74 mA h g⁻¹ in 26 cycles, and 3) SPSF-based battery exhibits greater stability with a capacity retention of 78.0%. Significantly, when the rate increases to 8 C (13.4 A g⁻¹), an unprecedentedly high rate for S-based batteries, the SPSF battery exhibits steady charge–discharge performance over 500 cycles with a capacity retention of 99.95% per cycle (Figure 2h). To determine membrane stability, additional characterizations were conducted after battery cycling tests. It is seen in Figure S11 in the Supporting Information that the membrane remains intact with no cracking. Importantly, chemical structure analysis in Figures S12 and S13 in the Supporting Information evidences no significant changes, confirming sufficient stability of the membrane. The practicability of the S–I₂ system was verified via connection of three cell units to power nine light emitting diodes (LEDs, 2.0 V, Figure 2i).

To investigate the significant difference in the performance of the three batteries, the ionic selectivity of the three membranes was assessed. This property is characterized by the cation transference number (t_+) that denotes the fraction of cation flow in the total cross-membrane ionic flux.^[23] A value of 1 indicates complete blockage of anion diffusion, while a value of 0.5 evidences no ionic selectivity.^[24] The t_+ value for the membrane is computed from Planck equation based on current–voltage (*I*–*V*) curves recorded in a two-compartment cell that has the membrane to separate the electrolyte with different concentrations (Figure S14, see Supporting information for details).^[25] Figure 3a presents the *I*–*V* curves for the cells with the membranes in the anodic Na₂S electrolyte under a concentration gradient of 10 × 10⁻³ M:1 × 10⁻³ M. The diffusion potential E_{diff} , represented by the intercept on the *I* = 0 axis, arises from the different diffusion rates of positive ions and negative ions and the resulting potential difference between the two solutions. The E_{diff} for SPSF exhibits a negative value, evidencing that cations permeate faster in the membrane.^[26] The t_+ value for the SPSF membrane is computed to be 0.97, higher than that for N117 of 0.83, evidencing stronger cation selectivity. For GF, the line passes through the origin, suggesting no cation preference. In the cathodic NaI₃ electrolyte (Figure 3b), the SPSF membrane also gives the highest transfer priority to Na⁺ with a t_+ value as high as 0.95, while the N117 membrane has a lower t_+ of 0.85. The GF membrane is nonselective with t_+ = 0.5. The *I*–*V* curves for SPSF under different concentration gradients are displayed in Figures S15 and S16 in the Supporting Information. It can be seen in Figure 3c that the membrane consistently exhibits a high t_+ value of >0.92.

To measure the permeability of polysulfides (S_x²⁻, 1 ≤ *x* ≤ 4) and triiodide (I₃⁻) through the membranes, static diffusion tests were determined in the two-compartment cells. The electrolyte was placed in the donating chamber, with deionized water placed in the receiving chamber. The concentration of anions in the water side was monitored via Ultraviolet-visible (UV-vis) spectroscopy and computed using pre-established standard concentration–absorbance equations (Figures S17–S20, Supporting Information). It is seen in Figure 3d that S₄²⁻ ions pass through GF readily and reach 0.43 × 10⁻³ M in the water side after resting for 13 min. The collecting side turns yellow-color as is visible in Figure S21 in the Supporting Information. S₄²⁻ ions penetrate N117 significantly more slowly but still rise to 0.88 × 10⁻³ M with the color change following 41 h rest (Figure 3e). The

SPSF membrane blocks S₄²⁻, and the water side remains “clear” after resting for 144 h. Similarly, for S₂²⁻ ions, they permeate across the GF membrane readily and accumulate to 50.75 × 10⁻³ M on the accepting side following 5.5 min (Figure 3f). The ions diffuse through the N117 membrane at a lower speed and increase to 3.57 × 10⁻³ M after 70 h. Importantly, no ions penetrate the SPSF membrane following 120 h. Analogous behavior is observed in S²⁻ diffusion, in which S²⁻ ions filter through the GF membrane at high speed and increase to 14.77 × 10⁻³ M after 120 s (Figure 3g). For the N117 film, the ion diffusion is slightly slower, but the concentration still increases to 4.04 × 10⁻³ M following 9 h. Significantly, the SPSF membrane restricts S²⁻ diffusion within 96 h. The effect of different membranes in suppressing I₃⁻ shuttling was assessed (Figure 3h). Compared with GF and N117, the SPSF membrane exhibits uncontaminated water over 120 h, confirming excellent ability in blocking I₃⁻ diffusion.

In addition to static diffusion testing, membrane permeability in electrochemical process was evaluated. In situ UV-vis spectrometry was used to monitor transmembrane diffusion of ions generated via electrode during operation. A quartz tube was used as a three-electrode cell with the working electrode and auxiliary electrode attached to two rough planes, with a Ag/AgCl reference electrode in between (inset photos in Figure 4a–d). GF and SPSF membranes were attached to the surface of the working electrode to impede ion diffusion. As depicted in Figure 4a, when the S electrode is discharging, the characteristic peaks of S₄²⁻ and S₂²⁻ at 300 and 368 nm are detected in solution, evidencing that the generated polysulfides pass through the GF membrane into electrolytes. As discharge proceeds, the peaks increase and the liquid turns yellow. Migrated polysulfides deplete the active material in the S electrode, rendering an irreversible redox reaction and a low charge capacity. This is also confirmed by the short charging time. In comparison, for the S system with SPSF membrane, the intensity of S₄²⁻ and S₂²⁻ detected in the electrolyte is significantly reduced, and the charging time is significantly prolonged, confirming the confinement of polysulfides (Figure 4b). For the NaI electrode with GF, the I₃⁻ peaks are immediately identified at 288 and 351 nm upon charging, followed by the I₂ signal at 440 nm (Figure 4c). These peaks rise as the charge proceeds and the solution turns deep yellow, indicating a drain of polyiodides into electrolytes. The loss of active materials in the electrode exhausts the capacity for discharge. With SPSF protecting the electrode, however, the UV-vis waves are negligible, and the reaction is highly reversible, evidencing a strong restraining of polyiodides on electrodes (Figure 4d). It is concluded that in situ UV-vis spectrometry assists to explain real-time transmembrane diffusion of anions, and confirms significant impact of the SPSF membrane in preventing anion leakage.

Because anion permeations are suppressed by the SPSF membrane, it is possible to study the complete evolution pathway of S and I₂ on their respective sides during operation. To identify reaction intermediates and explore conversion mechanism, in situ Raman spectrometry was used for two half cells. Figure 4e shows the phase evolution of the S anode during a charge–discharge cycle. At the beginning of charging, S₈ peaks are seen at 149, 215, and 468 cm⁻¹ (Figure S22, Supporting Information).^[27] They disappear at the tail of the first plateau, accompanied by emergence

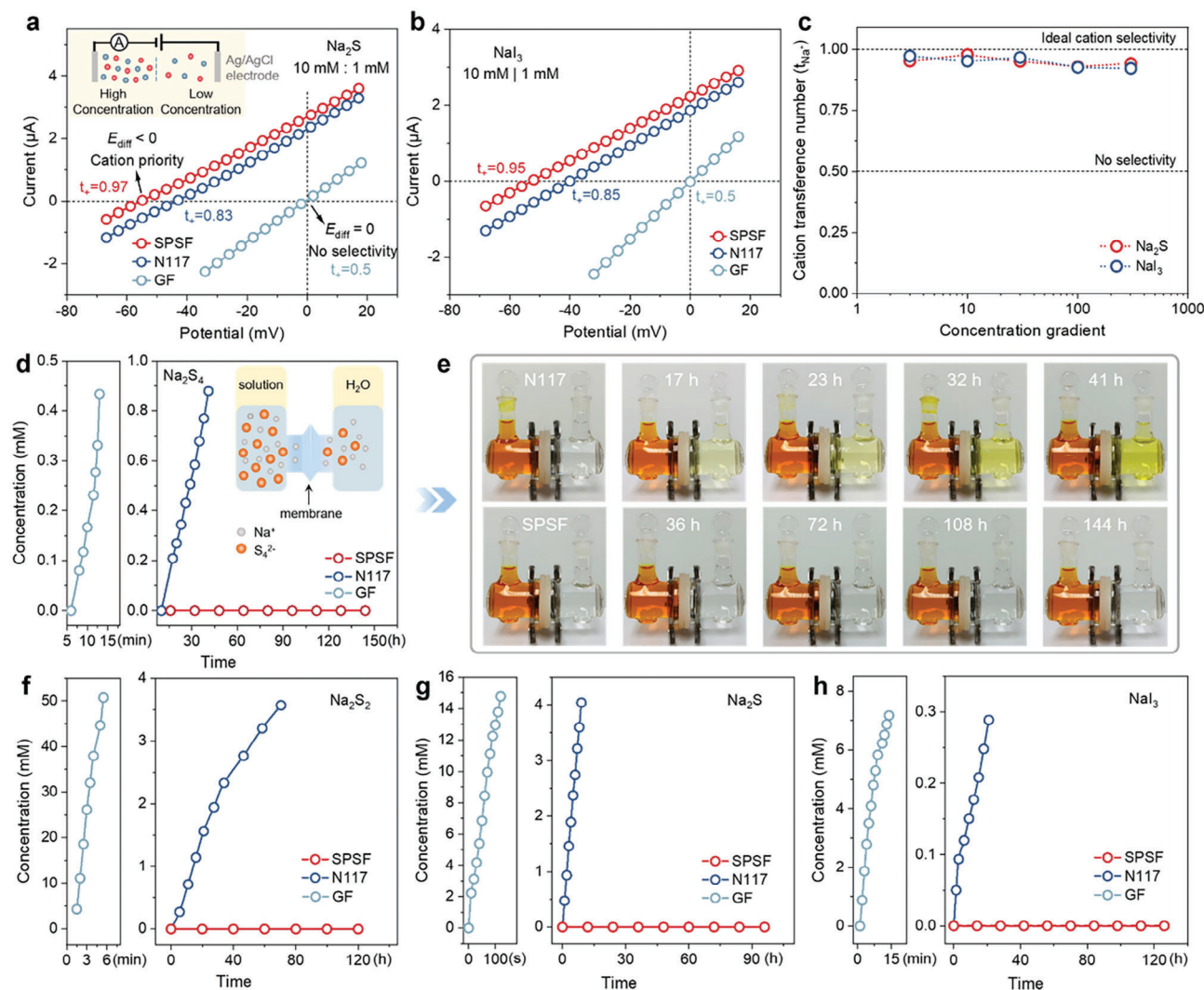


Figure 3. Ion selectivity of membranes and static diffusion of anions. Current–voltage (I – V) curves for the membranes in a) anodic Na_2S electrolyte and b) cathodic NaI_3 electrolyte. Inset is a schematic of the experimental apparatus. In both experiments, the concentration ratio of two compartments was $10 \times 10^{-3} \text{ M} : 1 \times 10^{-3} \text{ M}$. c) Cation transference numbers of the SPSF membrane under selected concentration gradients of Na_2S or NaI_3 electrolyte. d) Diffusion of Na_2S_4 through membranes measured in a two-compartment cell. Concentration of the receiving side is plotted as a function of time. e) Digital images of Na_2S_4 diffusion through Nafion (N117) and SPSF membrane at differing aging time. Concentration changes on the water side in diffusion tests for f) Na_2S_2 , g) Na_2S , and h) NaI_3 .

of polysulfide species. S_6^{2-} is observed from a broad peak from 280 to 400 cm^{-1} , with S_4^{2-} and S_5^{2-} sharing signals at 440 and 489 cm^{-1} .^[28] The peaks at 192, 245, and 419 cm^{-1} are attributed to S_4^{2-} , while signals at 150 and 215 cm^{-1} are ascribed to S_5^{2-} .^[28,29] In the second plateau of charge, the peaks of S_5^{2-} and S_6^{2-} vanish, and S_3^{2-} signals appear at 230 and 466 cm^{-1} .^[29a] In the latter half, S_4^{2-} and S_3^{2-} transform to S_2^{2-} with the relevant peak appearing at 446 cm^{-1} .^[28b] At the end of charge, S_2^{2-} changes to S^{2-} and its signal disappears, evidencing a complete conversion from S_8 to S^{2-} . The reaction is consistent with reported mechanism that the first reduction plateau represents conversion from elemental S to long-chain polysulfides (S_x^{2-} , $4 \leq x \leq 8$), and the second signifies transition to short-chain polysulfides (S_x^{2-} , $1 \leq x \leq 4$).^[1a,5b] During subsequent discharging, the S_2^{2-} peak increases initially, followed by regeneration of S_4^{2-} and final product S_8 ,

confirming highly reversible electrochemical behavior. Figure 4f presents the spectra changes of the NaI cathode when an excess S anode is used to ensure full utilization of NaI. In charging, I_3^- and I_5^- peaks appear at, respectively, 103 and 161 cm^{-1} (Figure S23, Supporting Information).^[20a] The I_3^- signal strengthens initially and then slowly decreases for conversion to I_5^- . The I_5^- signal reaches a maximum near the middle of the second plateau and then steadily decreases, indicating its oxidation to I_2 . In discharging, I_3^- and I_5^- are regenerated in the early stage. The peaks fade with time, evidencing a consecutive reduction to I^- . The entire evolution follows the highly reversible reaction, $\text{I}^- \leftrightarrow \text{I}_3^- \leftrightarrow \text{I}_5^- \leftrightarrow \text{I}_2$.

To establish practical feasibility of the S– I_2 battery, the performance was compared directly with a Zn– I_2 battery. In situ differential electrochemical mass spectrometry (DEMS) was

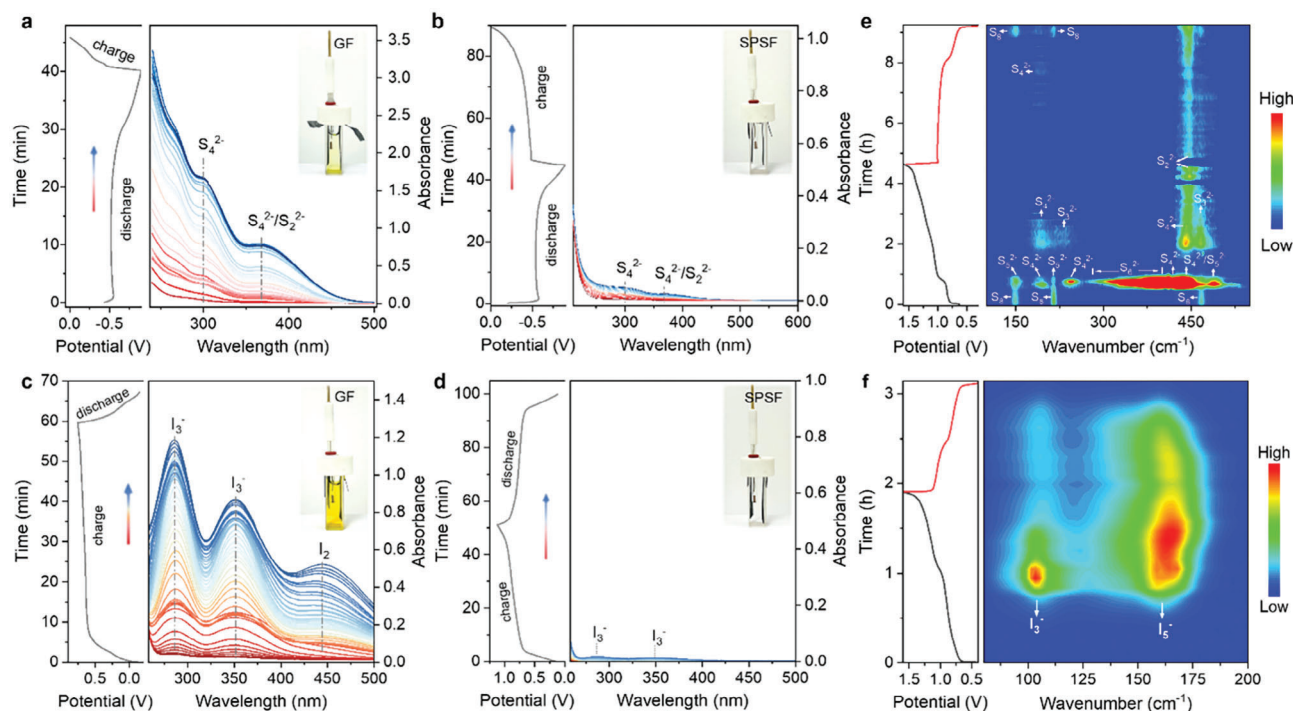


Figure 4. In situ spectrometry analyses of transmembrane diffusion and electrode reaction pathway. In situ UV-vis spectrometry monitoring of polysulfides permeation through a) glass fiber (GF) and b) SPSF membrane when S electrode was discharging and charging. In situ UV-vis recording of triiodides permeation through c) GF and d) SPSF membrane when NaI electrode was charging and discharging. In situ Raman spectra of e) S anode and f) NaI cathode in S-I₂ battery with SPSF membrane.

used on half cells in Zn-I₂ system and S-I₂ battery to detect gas release (Figure S24, Supporting Information). In Figure 5a,b, the potential of oxygen evolution reaction in the two batteries of 0.97 V is significantly different to that for I⁻ oxidation of 0.52 V, evidencing a gas-free cathode. However, HER in the Zn-I₂ cell occurs at -0.87 V, which closely neighbors the onset potential for Zn plating of -0.84 V. Findings evidence that HER is highly competitive and can occur concurrently with Zn deposition during battery operation. This can lead to reduced efficiency, uneven plating, by-product formation (e.g., ZnO/Zn(OH)₂), excessive internal pressure, and even cracking of battery package. HER in the S-I₂ cell, however, is not observed until the voltage is scanned to -1.14 V, significantly distant from the S reduction potential of -0.56 V. As a result, the use of S anode circumvents HER to ensure an efficient and safe battery.

Electrode utilization, or DoD, significantly affects lifespan and energy density of a battery. However, in most reported research on Zn-ion batteries (ZIBs), excessive Zn is used (e.g., Zn foil with a thickness of 100 μm, equivalent to 58.5 mA h cm⁻²), resulting in a significantly low DoD of < 1%. Although such use provides boosted cycling performance, it is not practically applicable because a battery needs to minimize the mass of surplus electrode materials to give greater gravimetric energy density. To establish the significant impact of low Zn DoD on energy density of ZIBs, a graphical comparison is presented in Figure 5c-e. With an ideal 100% DoD (Figure 5c), most ZIBs have an energy density of >100 W h kg⁻¹ (based on the active materials of cathode and anode), e.g., Zn-I₂ battery exhibits an energy density of 206 W h kg⁻¹. However, as the DoD decreases

to 50%, most batteries decline to ≤200 W h kg⁻¹. When only 10% of the anode is utilized, the energy density of all batteries drops to ≤100 W h kg⁻¹, with Zn-I₂ battery showing a significant reduction to 73 W h kg⁻¹, representing an ≈65% reduction compared to 100% DoD. Given actual utilization reported is lower, there is still a long way to go for ZIBs to fulfill the energy promise.

S anode, however, withstands high utilization to exhibit desired capacity. To illustrate this, the performance of Zn-I₂ battery and S-I₂ battery under selected DoD was compared. Figure S25 in the Supporting Information presents cycling performance of a Zn-I₂ battery at 0.85% DoD that demonstrates excellent cycling stability with 98.1% capacity retention over 3000 cycles. However, when the DoD increases to 50%, the capacity begins to decrease after 130 cycles, and it drops to 28.9% after 500 cycles (Figure 5f and Figure S26, Supporting Information). At a DoD of 75%, a significant capacity reduction of 50% is apparent within the first 50 cycles, followed by a gradual decrease to 9.9% (Figure S27, Supporting Information). Once the Zn anode is fully utilized, its capacity decreases to 25% within 200 cycles and to ≈0 after 300 cycles (Figure S28, Supporting Information). In contrast, the S anode exhibits significant durability. Under a DoD of 50%, its capacity remains nearly constant over 500 cycles with a decrease of only 1.9% (Figure 5g). At 100% utilization, the battery maintains 87.6% of its capacity after 500 cycles. These quantitative findings confirm that the S anode will meet the demanding requirements in practical working conditions. A S-I₂ pouch cell was assembled and tested under a high current of 1.8 A. In Figure 5h, the cell exhibits a slight capacity decrease

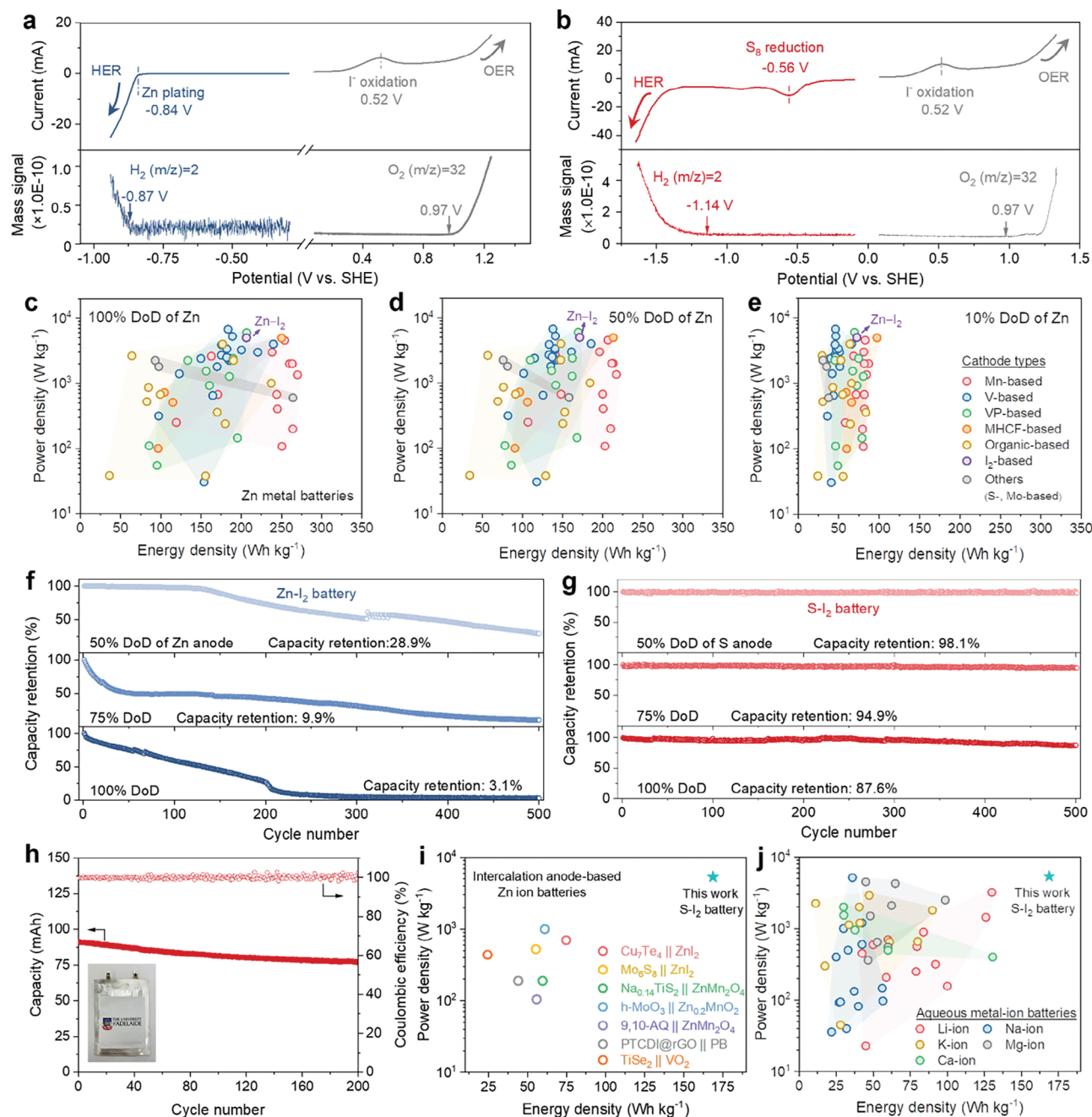


Figure 5. Comparison of Zn and S anode, and evaluation of the pouch cell. DEMS characterizations to detect gas release in half cells of a) Zn-I₂ battery and b) S-I₂ battery. Power density and energy density of typical reported Zn-ion batteries (ZIBs) computed at c) 100%, d) 50%, and e) 10% utilization of Zn anode. Capacity retention over cycles of f) Zn-I₂ and g) S-I₂ battery under 50%, 75%, and 100% utilization of anode. h) Cycling stability of S-I₂ pouch cell. Comparison of findings with i) intercalation-anode-based ZIBs and j) selected aqueous metal-ion (Li⁺, Na⁺, K⁺, Ca²⁺, and Mg²⁺) batteries.

because of the super-high mass loading of NaI of $\approx 37 \text{ mg cm}^{-2}$, yielding an overall 84.9% capacity retention over 200 cycles. The S-I₂ battery is compared with state-of-the-art aqueous systems in Figure 5i,j. The S-I₂ battery exhibits an energy density of up to 168.8 Wh kg^{-1} and a power density of 5360 W kg^{-1} , greater than that of intercalation anode-based ZIBs and aqueous metal-ions (Li⁺, Na⁺, K⁺, Ca²⁺, and Mg²⁺) batteries, evidencing its practical potential.

3. Conclusion

We presented S as a promising anode candidate and demonstrated its potential in S-I₂ batteries by designing an SPSF membrane that effectively reduced polysulfide/iodide crossover. Importantly, the membrane is priced at $\$1.82 \text{ m}^{-2}$ and free from fluorine pollution, and is therefore a practical alternative to commercial Nafion membranes that cost $>\$3500 \text{ m}^{-2}$.

The membrane exhibited high cation selectivity with cation transfer numbers of >0.92 , significantly improving battery charge–discharge reversibility and efficiency. With a close-to-theoretical discharge capacity of 1404 mA h g^{-1} , our battery outperformed those based on N117 and GF that exhibited, respectively, 724 and 127 mA h g^{-1} . The effectiveness of SPSF membrane in suppressing both polysulfides and polyiodides shuttling was confirmed in situ via UV-vis during electrode operation. Significantly, the SPSF-based battery maintained stable running even at a record-high rate of 8 C (13.4 A g^{-1}), exhibiting an excellent capacity retention of 99.95% per cycle. A pouch cell with a super-high mass loading of $\approx 37 \text{ mg cm}^{-2}_{\text{NaI}}$ exhibited high stability as evidenced by a capacity retention of 84.9% over 200 cycles. More importantly, the superiority of S anode over Zn was emphasized. In situ DEMS confirmed that the S anode exhibited a significantly higher reduction potential than HER, in contrast to Zn plating that readily initiated unwanted gas evolution. In comparison with metallic Zn anode, S anode exhibited 100% utilization with cycling stability that contributed to high energy density output. We conclude therefore that these findings provide a practical anode beyond metals for high-energy, low-cost, and fast-chargeable batteries. Findings will benefit the design of aqueous batteries and be of interest to a range of researchers and device manufacturers.

Supporting Information

Supporting Information is available from the Wiley Online Library or from the author.

Acknowledgements

Q.C. and J.H. contributed equally to this work. This work was sponsored by Australian Research Council (DP220102596, LP210301397, DE230100471, IH200100035 and IL230100039). The authors also acknowledge the Australian Institute of Nuclear Science and Engineering (AINSE) support through Early Career Researcher Grant (ECRG, J.H.). [Correction added on 4 December 2023, after first online publication: CAUL funding statement has been added.]

Open access publishing facilitated by The University of Adelaide, as part of the Wiley - The University of Adelaide agreement via the Council of Australian University Librarians.

Conflict of Interest

The authors declare no conflict of interest.

Data Availability Statement

The data that support the findings of this study are available from the corresponding author upon reasonable request.

Keywords

aqueous batteries, membranes, shuttle effects, sulfur anodes

Received: September 4, 2023

Revised: November 2, 2023

Published online: November 21, 2023

- [1] a) J. Liu, W. Zhou, R. Zhao, Z. Yang, W. Li, D. Chao, S.-Z. Qiao, D. Zhao, *J. Am. Chem. Soc.* **2021**, *143*, 15475; b) Z. Yang, C. Xu, M. Xia, X. Zhang, H. Yan, H. Yu, T. Sun, L. Zhang, F. Hu, J. Shu, *Mater. Today* **2021**, *49*, 184.
- [2] Z. W. Seh, Y. Sun, Q. Zhang, Y. Cui, *Chem. Soc. Rev.* **2016**, *45*, 5605.
- [3] a) W. Li, K. Wang, K. Jiang, *Adv. Sci.* **2020**, *7*, 2000761; b) J. Liu, C. Ye, H. Wu, M. Jaroniec, S.-Z. Qiao, *J. Am. Chem. Soc.* **2023**, *145*, 5384; c) M. Yang, Z. Yan, J. Xiao, W. Xin, L. Zhang, H. Peng, Y. Geng, J. Li, Y. Wang, L. Liu, Z. Zhu, *Angew. Chem., Int. Ed.* **2022**, *61*, e202212666; d) D. Liu, B. He, Y. Zhong, J. Chen, L. Yuan, Z. Li, Y. Huang, *Nano Energy* **2022**, *101*, 107474; e) W. Zhang, M. Wang, J. Ma, H. Zhang, L. Fu, B. Song, S. Lu, K. Lu, *Adv. Funct. Mater.* **2023**, *33*, 2210899; f) M. Cui, J. Fei, F. Mo, H. Lei, Y. Huang, *ACS Appl. Mater. Interfaces* **2021**, *13*, 54981.
- [4] a) X. Wu, A. Markir, Y. Xu, E. C. Hu, K. T. Dai, C. Zhang, W. Shin, D. P. Leonard, K.-I. Kim, X. Ji, *Adv. Energy Mater.* **2019**, *9*, 1902422; b) X. Wu, A. Markir, L. Ma, Y. Xu, H. Jiang, D. P. Leonard, W. Shin, T. Wu, J. Lu, X. Ji, *Angew. Chem., Int. Ed.* **2019**, *58*, 12640; c) C. Xu, Z. Yang, H. Yan, J. Li, H. Yu, L. Zhang, J. Shu, *Proc. Natl. Acad. Sci. U. S. A.* **2022**, *119*, e2118675119.
- [5] a) S. Yun, S. H. Park, J. S. Yeon, J. Park, M. Jana, J. Suk, H. S. Park, *Adv. Funct. Mater.* **2018**, *28*, 1707593; b) N. Li, Z. Weng, Y. Wang, F. Li, H.-M. Cheng, H. Zhou, *Energy Environ. Sci.* **2014**, *7*, 3307.
- [6] J. Hao, L. Yuan, B. Johannessen, Y. Zhu, Y. Jiao, C. Ye, F. Xie, S.-Z. Qiao, *Angew. Chem., Int. Ed.* **2021**, *60*, 25114.
- [7] J. Hao, L. Yuan, Y. Zhu, M. Jaroniec, S.-Z. Qiao, *Adv. Mater.* **2022**, *34*, 2206963.
- [8] C. Li, S. Jin, L. A. Archer, L. F. Nazar, *Joule* **2022**, *6*, 1733.
- [9] M. Kumar, A. K. Padhan, D. Mandal, T. C. Nagaiah, *Energy Storage Mater.* **2022**, *45*, 1052.
- [10] a) J. Shao, X. Li, L. Zhang, Q. Qu, H. Zheng, *Nanoscale* **2013**, *5*, 1460; b) X. Wu, X. Yuan, J. Yu, J. Liu, F. Wang, L. Fu, W. Zhou, Y. Zhu, Q. Zhou, Y. Wu, *Nanoscale* **2017**, *9*, 11004.
- [11] C. Yang, L. Suo, O. Borodin, F. Wang, W. Sun, T. Gao, X. Fan, S. Hou, Z. Ma, K. Amine, K. Xu, C. Wang, *Proc. Natl. Acad. Sci. U. S. A.* **2017**, *114*, 6197.
- [12] C. Wei, Y. Wang, Z. Ding, T. Fang, J. Song, Y. Zhang, S. Lv, X. Liu, X. Tang, *Adv. Funct. Mater.* **2023**, *33*, 2212644.
- [13] M. Feng, R. Qu, Z. Wei, L. Wang, P. Sun, Z. Wang, *Sci. Rep.* **2015**, *5*, 9859.
- [14] a) M. S. Pan, L. Su, S. L. Eiler, L. W. Jing, A. F. Badel, Z. Li, F. R. Brushett, Y.-M. Chiang, *J. Electrochem. Soc.* **2022**, *169*, 060524; b) Z. Li, G. Weng, Q. Zou, G. Cong, Y.-C. Lu, *Nano Energy* **2016**, *30*, 283.
- [15] a) Y. Zhang, L. Zheng, B. Liu, H. Wang, H. Shi, *J. Membr. Sci.* **2019**, *584*, 173; b) C. G. Arges, V. Ramani, *Proc. Natl. Acad. Sci. U. S. A.* **2013**, *110*, 2490.
- [16] Y. Zhao, X. Wang, Y. Ren, D. Pei, *ACS Appl. Mater. Interfaces* **2018**, *10*, 2918.
- [17] Y. Tang, Z. Xue, X. Zhou, X. Xie, C.-Y. Tang, *Sens. Actuators, B* **2014**, *202*, 1164.
- [18] P. Zuo, Z. Xu, Q. Zhu, J. Ran, L. Ge, X. Ge, L. Wu, Z. Yang, T. Xu, *Adv. Funct. Mater.* **2022**, *32*, 2207366.
- [19] C. Wei, W. Yu, L. Wu, X. Ge, T. Xu, *Polymers* **2022**, *14*, 4920.
- [20] a) S.-J. Zhang, J. Hao, H. Li, P.-F. Zhang, Z.-W. Yin, Y.-Y. Li, B. Zhang, Z. Lin, S.-Z. Qiao, *Adv. Mater.* **2022**, *34*, 2201716; b) L. Yan, S. Zhang, Q. Kang, X. Meng, Z. Li, T. Liu, T. Ma, Z. Lin, *Energy Storage Mater.* **2023**, *54*, 339; c) D. Lin, Y. Li, *Adv. Mater.* **2022**, *34*, 2108856.
- [21] a) Y. Zhu, K. He, T. Tadesse Tsaga, N. Ali, J. Zai, S. Huang, X. Qian, Z. Chen, *Sustainable Energy Fuels* **2020**, *4*, 2892; b) Z. Li, Y.-C. Lu, *Nat. Energy* **2021**, *6*, 517; c) M. Rahimi, A. Molaei Dehkordi, E. P. L. Roberts, *Electrochim. Acta* **2021**, *369*, 137687; d) L. Su, A. F. Badel, C. Cao, J. J. Hinricher, F. R. Brushett, *Ind. Eng. Chem. Res.* **2017**, *56*, 9783; e) J. Zai, Y. Zhu, K. He, A. Iqbal, S. Huang, Z. Chen, X. Qian, *Mater. Chem.*

- Phys.* **2020**, 250, 123143; f) Y. Qin, X. Li, W. Liu, X. Lei, *Mater. Today Energy* **2021**, 21, 100746; g) D. Ma, B. Hu, W. Wu, X. Liu, J. Zai, C. Shu, T. Tadesse Tsega, L. Chen, X. Qian, T. L. Liu, *Nat. Commun.* **2019**, 10, 3367.
- [22] H. B. Park, J. Kamcev, L. M. Robeson, M. Elimelech, B. D. Freeman, *Science* **2017**, 356, eaab0530.
- [23] Q. Zhu, Y. Li, Q. Qian, P. Zuo, M. D. Guiver, Z. Yang, T. Xu, *Energy Environ. Sci.* **2022**, 15, 4148.
- [24] J. Zhou, Z. Jiao, Q. Zhu, Y. Li, L. Ge, L. Wu, Z. Yang, T. Xu, *J. Membr. Sci.* **2021**, 627, 119246.
- [25] R. H. Tunuguntla, R. Y. Henley, Y.-C. Yao, T. A. Pham, M. Wanunu, A. Noy, *Science* **2017**, 357, 792.
- [26] D.-K. Kim, C. Duan, Y.-F. Chen, A. Majumdar, *Microfluid. Nanofluid.* **2010**, 9, 1215.
- [27] H. Li, R. Meng, Y. Guo, B. Chen, Y. Jiao, C. Ye, Y. Long, A. Tadich, Q.-H. Yang, M. Jaroniec, S.-Z. Qiao, *Nat. Commun.* **2021**, 12, 5714.
- [28] a) G. J. Janz, J. W. Coutts, J. R. Downey, E. Roduner, *Inorg. Chem.* **1976**, 15, 1755; b) H. Hermann Eysel, G. Wiegardt, H. Kleinschmager, G. Weddigen, *Z. Naturforsch., B: J. Chem. Sci.* **1976**, 31, 415.
- [29] a) G. J. Janz, J. R. Downey, E. Roduner, G. J. Wasilczyk, J. W. Coutts, A. Eluard, *Inorg. Chem.* **1976**, 15, 1759; b) H. Ziemann, W. Buss, *Z. Anorg. Allg. Chem.* **1979**, 455, 69; c) A. T. Ward, *Mater. Res. Bull.* **1969**, 4, 581.